Comput Geosci (2008) 12:257–272
DOI 10.1007/s10596-007-9073-7

ORIGINAL PAPER

Multiscale simulations of porous media flows in flow-based coordinate system

Y. Efendiev · T. Hou · T. Strinopoulos

Received: 2 April 2006 / Accepted: 10 September 2007 / Published online: 6 March 2008

Abstract In this paper, we propose a multiscale technique for the simulation of porous media flows in a flow-based coordinate system. A flow-based coordinate system allows us to simplify the scale interaction and derive the upscaled equations for purely hyperbolic transport equations. We discuss the applications of the method to two-phase flows in heterogeneous porous media. For two-phase flow simulations, the use of a flow-based coordinate system requires limited global information, such as the solution of single-phase flow. Numerical results show that one can achieve accurate upscaling results using a flow-based coordinate system.

Keywords Porous media flow · Flow-based coordinate system · Two-phase flow · Multiscale · Upscaling

1 Introduction

The modeling of two-phase flow in porous formations is important for both environmental remediation and the management of petroleum reservoirs. Practical situations involving two-phase flow include the dispersal of a nonaqueous phase liquid in an aquifer or the displacement of a nonaqueous phase liquid by water. In the subsurface, these processes are complicated by the effects of permeability heterogeneity on the flow and transport. Simulation models, if they are to provide realistic predictions, must accurately account for these effects. However, because permeability heterogeneity occurs at many different length scales, numerical flow models cannot in general resolve all of the scales of variation. Therefore, approaches are needed for representing the effects of subgrid scale variations on larger-scale flow results. Typically, upscaled or multiscale models are employed for such systems. The main idea of upscaling techniques is to form coarse-scale equations with a prescribed analytical form that may differ from the underlying fine-scale equations. In multiscale methods, the fine-scale information is carried throughout the simulation and the coarse-scale equations are generally not expressed analytically but, rather, formed and solved numerically.

On the fine (fully resolved) scale, the subsurface flow and transport of N components can be described in terms of an elliptic (for incompressible systems) pressure equation coupled to a sequence of $N-1$ hyperbolic (in the absence of dispersive and capillary pressure effects) conservation laws. Our purpose in this paper is to perform upscaling of two-phase immiscible flow in a flow-based coordinate system. The flow-based coordinate system provides us with a solution that is better suited for upscaling because the solution is smoother and the scale interaction can be simpler. We would like to note that single-phase flow upscaling methods have been employed in the Cartesian framework using flow-based grids [25]. In flow-based grid

Y. Efendiev (✉)
Department of Mathematics, Texas A&M University,
College Station, TX 77843-3368, USA
e-mail: efendiev@math.tamu.edu

T. Hou · T. Strinopoulos
Applied Mathematics, Caltech, Pasadena, CA 91125, USA

T. Hou
e-mail: hou@acm.caltech.edu

T. Strinopoulos
e-mail: theofilos@acm.caltech.edu

upscaling, the original equations are solved in a flow-based grid generated using the streamlines of the flow. Because of the similarities with the upscaling in flow-based grid, we use the terminology "flow-based coordinate system." The use of flow-based coordinate system allows us to perform accurate upscaling of the transport equation, which is purely hyperbolic. The upscaling of the transport equation along the streamlines in the current pressure-streamline coordinate system can be obtained because the equation is one-dimensional. We discuss the upscaling of the saturation equation across the streamlines. This type of upscaling introduces nonlocal macrodispersion terms, where the macrodispersion term involves two-point correlation of the velocity field along the streamlines. The advantage of using the flow-based coordinate system is that the computation of macrodispersion can be performed semianalytically. This allows us to avoid the typical difficulties [13] associated with the computation of the macrodiffusion term, including cross diffusion terms.

For upscaling of the pressure equation, we employ multiscale finite element type methods (MsFEM). MsFEM was first introduced in Hou and Wu [16]. Its main idea is to incorporate the small-scale information into finite element basis functions and capture their effect on the large scale via finite element computations. This approach shares common features with a number of other multiscale numerical methods, such as residual free bubbles [6, 22], variational multiscale method [18], MsFEM [16], two-scale finite element methods [21], and two-scale conservative subgrid approaches [2]. We remark that special basis functions in finite element methods have been used earlier in Babuška and Osborn [3] (cf. [4]). Multiscale finite element methodology has been modified and successfully applied to two-phase flow simulations in Jenny et al. [19, 20] and Aarnes [1] and later in Chen and Hou [8]. Arbogast [2] used variational multiscale strategy and constructed a multiscale method for two-phase flow simulations. When considering two-phase flow upscaling, we use multiscale basis functions to compute the macrodispersion. Recently, a limited global information has been used [1, 11] in constructing multiscale basis functions. It is interesting to note that, in the flow-based coordinate system, these multiscale methods reduce to a standard multiscale finite element method [16].

The paper is organized in the following way: In the next section, we present the governing equations. In Section 3, we briefly present a motivation for our approach. Section 4 is devoted to the upscaling of transport equation (hyperbolic equation). In Section 5, we briefly mention multiscale finite element methods. The numerical results are presented in Section 6.

2 Fine-scale equations

We consider two-phase flow in a reservoir Ω under the assumption that the displacement is dominated by viscous effects; i.e., we neglect the effects of gravity, compressibility, and capillary pressure. Porosity will be considered to be constant. The two phases will be referred to as water and oil, designated by subscripts w and o, respectively. We write Darcy's law, with all quantities dimensionless, for each phase as follows:

$$\mathbf{v}_j = -\frac{k_{rj}(S)}{\mu_j}\mathbf{k}\cdot\nabla P, \tag{1}$$

where $\mathbf{v}_j$ is the phase velocity, $\mathbf{k}$ is the permeability tensor, k_{rj} is the relative permeability to phase $j\,(j=o,w)$, S is the water saturation (volume fraction), P is pressure, and μ_j is the viscosity of phase $j\,(j=0,w)$. In this work, a single set of relative permeability curves is used and $\mathbf{k}$ is assumed to be a diagonal tensor. Combining Darcy's law with a statement of conservation of mass allows us to express the governing equations in terms of the so-called pressure and saturation equations:

$$\nabla\cdot(\lambda(S)\mathbf{k}\cdot\nabla P) = q, \tag{2}$$

$$\frac{\partial S}{\partial t} + \mathbf{v}\cdot\nabla f(S) = 0, \tag{3}$$

where λ is the total mobility, f is the fractional flow of water, q is a source term, and $\mathbf{v}$ is the total velocity, which are respectively given by:

$$\lambda(S) = \frac{k_{rw}(S)}{\mu_w} + \frac{k_{ro}(S)}{\mu_o},$$

$$f(S) = \frac{k_{rw}(S)/\mu_w}{k_{rw}(S)/\mu_w + k_{ro}(S)/\mu_o}, \tag{4}$$

$$\mathbf{v} = \mathbf{v}_w + \mathbf{v}_o = -\lambda(S)\mathbf{k}\cdot\nabla P. \tag{5}$$

The above descriptions are referred to as the fine model of the two-phase flow problem. For simplicity, in further analyses, we will assume $q=0$ and impose nonhomogeneous boundary conditions.

3 Motivation

The upscaling and multiscale methods for two-phase flow systems have been discussed by many authors. In most upscaling procedures, the upscaled quantities are computed on a coarse grid obtained from the underlying fine-grid. Because of strong scale interactions associated with complex spatial correlations, most upscaling and multiscale methods may require some type

of global information or border regions to take into account nonlocal neighboring information. In the proposed work, multiscale, and upscaling techniques are used in a flow-based coordinate system. This coordinate system, which is based on limited global information, can provide additional smoothness for the solution, and it simplifies the scale interaction.

Next, we present the flow-based coordinate system and the modified equation and discuss some asymptotic properties of the modified equations in the flow-based coordinate system. We will restrict our analysis to the two-dimensional case and assume that the heterogeneous porous medium is isotropic, $\mathbf{k}(\mathbf{x}) = k(\mathbf{x})\mathbf{I}$. In general, the stream function is defined as $\nabla \times \psi = \mathbf{v} = (v_1, v_2)$. In two dimensions, the stream function ψ reduces to a scalar field defined by

$$\partial\psi/\partial x_1 = -v_2, \quad \partial\psi/\partial x_2 = v_1. \tag{6}$$

It can be easily shown that $\nabla\psi \cdot \nabla p = 0$, where p is initial pressure. Denote the initial stream function and pressure by $\psi = \psi(x, t = 0)$ and $p = P(x, t = 0)$. If we assume $S = 0$ at time zero, then (ψ, p) can be obtained from the pressure equation with $\lambda(S) = 1$. Then, the equation for pressure and stream function can be written down in this curvilinear orthogonal coordinate system using standard coordinate transformation techniques (see [11, 23]). As a result, we obtain

$$\frac{\partial}{\partial\psi}\left(k^2\lambda(S)\frac{\partial P}{\partial\psi}\right) + \frac{\partial}{\partial p}\left(\lambda(S)\frac{\partial P}{\partial p}\right) = 0. \tag{7}$$

Applying the same change of variables to saturation equation, we get

$$\frac{\partial S}{\partial t} + (\mathbf{v}\cdot\nabla\psi)\frac{\partial f(S)}{\partial\psi} + (\mathbf{v}\cdot\nabla p)\frac{\partial f(S)}{\partial p} = 0. \tag{8}$$

Our objective is to present an upscaling method in pressure-streamline framework for two-phase flow equations. The cornerstone of our upscaling method is the fact that the pressure at later times is a smooth function of initial pressure and, thus, the upscaling of initial pressure-streamline framework is more robust and accurate. In Efendiev et al. [11], the authors consider a special case when the permeability has strong nonlocal effects with a single high-permeability channel. The authors show that, in this case, the pressure evolution can be written as

$$P(\psi, p, t) = P_0(p, t) + h.o.t, \tag{9}$$

where P_0 is the solution of

$$\frac{\partial}{\partial p}\left(\lambda_0(p, t)\frac{\partial P_0}{\partial p}\right) = 0, \tag{10}$$

where λ_0 depends S_0. If λ is a smooth function, then P_0 is a smooth function with respect to p. Here, $h.o.t$ are related to the contrast in the permeability field, which is very high inside the channel. This expansion shows that, in porous media with strong channelized nonlocal effects, the initial pressure-streamline coordinate system can provide a better coordinate system for performing upscaling. First, this coordinate system can simplify the scale interaction and nonlocal effects can be modeled more accurately.

4 Upscaling of saturation equation in flow-based coordinate system

4.1 Homogenization of saturation equation

In this section, we would like to derive an upscaled model for the transport equation. We will assume that the velocity is independent of time, $\lambda(S) = 1$, and restrict ourselves to the two-dimensional case. Then, using the pressure-streamline framework, one obtains

$$\begin{aligned} &S^\epsilon_t + v^\epsilon_0 f(S^\epsilon)_p = 0 \\ &S(p, \psi, t = 0) = S_0, \end{aligned} \tag{11}$$

where ϵ denotes the small scale and v^ϵ_0 denotes the Jacobian of the transformation and is positive. For simplicity, we assume $\mathbf{k}(\mathbf{x}) = k(\mathbf{x})\mathbf{I}$ and we have $\nabla\psi \cdot \nabla p = 0$. For deriving upscaled equations, we will first homogenize Eq. 11 along the streamlines, and then homogenize across the streamlines. The homogenization along the streamlines can be done following Bourgeat and Mikelić [5] or following Hou and Xin [17] and Weinan [10]. The latter uses two-scale convergence theory, and we refer to Strinopoulos [23] for the results on homogenization of Eq. 11 using two-scale convergence theory. We note that the homogenization results of Bourgeat and Mikelic are for general heterogeneities without an assumption on periodicity, and thus, they are more appropriate for problems considered in the paper. Following Bourgeat and Mikelić [5], the homogenization of Eq. 11 can be easily derived (see Proposition 3.4 in [5]).

For ease of notations, we ignore the ψ dependence of v^ϵ_0 and S^ϵ and treat ψ as a parameter. We consider

$$v^\epsilon_0(p) = v_0\left(p, \frac{p}{\epsilon}\right),$$

where the velocity field has both large-scale and small-scale variations. Moreover, we assume that the domain is a unit interval. Then, for each ψ, it can be shown that

$S^\epsilon(p,\psi,t) \to \tilde{S}(p,\psi,t)$ in $L^1((0,1)\times(0,T))$, where $\tilde{S}$ satisfies

$$\tilde{S}_t + \tilde{v}_0 f(\tilde{S})_p = 0, \tag{12}$$

and where $\tilde{v}_0$ is harmonic average of v_0^ϵ, i.e.,

$$\frac{1}{v_0^\epsilon} \to \frac{1}{\tilde{v}_0} \quad \text{weak} * \text{ in } L^\infty(0,1),$$

as $\epsilon \to 0$. The proof of this fact follows from Proposition 3.4. of Bourgeat and Mikelić [5]. Here, we briefly sketch the proof.

Following Bourgeat and Mikelić [5] and assuming for simplicity $\int_0^1 \frac{d\eta}{v_0^\epsilon(\eta)} = \int_0^1 \frac{d\eta}{\tilde{v}_0(\eta)} = 1$, we introduce

$$\frac{dX^\epsilon(p)}{dp} = v_0^\epsilon(X^\epsilon(p)), \qquad \frac{dX^0(p)}{dp} = \tilde{v}_0(X^0(p)).$$

Then (Lemma 3.1 of Bourgeat and Mikelić [5]):

$$X^\epsilon \to X^0 \quad \text{in } C[0,1] \text{ as } \epsilon \to 0. \tag{13}$$

Consequently,

$$\begin{aligned}
&\int_0^T\int_0^1 |S^\epsilon(p,\tau) - \tilde{S}(p,\tau)|dpd\tau \\
&= \int_0^T\int_0^1 |S^\epsilon(X^\epsilon(p),\tau) - \tilde{S}(X^\epsilon(p),\tau)|v_0^\epsilon(X^\epsilon(p))dpd\tau \\
&\le \int_0^T\int_0^1 |S^\epsilon(X^\epsilon(p),\tau) - \tilde{S}(X^0(p),\tau)|v_0^\epsilon(X^\epsilon(p))dpd\tau \\
&\quad + \int_0^T\int_0^1 |\tilde{S}(X^\epsilon(p),\tau) - \tilde{S}(X^0(p),\tau)|v_0^\epsilon(X^\epsilon(p))dpd\tau \\
&\le \int_0^T\int_0^1 |S^\epsilon(X^\epsilon(p),\tau) - \tilde{S}(X^0(p),\tau)|dpd\tau \\
&\quad + \int_0^T\int_0^1 |\tilde{S}(X^\epsilon(p),\tau) - \tilde{S}(X^0(p),\tau)|dpd\tau
\end{aligned} \tag{14}$$

The first term on the right-hand side of Eq. 14 converges to zero because $S^\epsilon(X^\epsilon(p),\tau)$ and $\tilde{S}(X^0(p),\tau)$ satisfy the same equation $u_t + f(u)_p = 0$, however, with the following initial conditions $S^\epsilon(X^\epsilon(p), t=0) = S_0 \circ X^\epsilon$ $\tilde{S}(X^0(p),\tau) = S_0 \circ X^0$. Because of Eq. 13 and comparison principle

$$\begin{aligned}
&\int_0^T\int_0^1 |S^\epsilon(X^\epsilon(p),\tau) - \tilde{S}(X^0(p),\tau)|dpd\tau \\
&\le C\int_0^1 |S_0 \circ X^\epsilon - S_0 \circ X^0|dp,
\end{aligned}$$

the first term converges to zero. The convergence of the second term for each ψ follows from the argument in Bourgeat and Mikelić ([5], page 368) using Lebesgue's dominated convergence theorem.

Next, we provide a convergence rate (see also [23]) of the fine saturation S^ϵ to the homogenized limit $\tilde{S}$ as $\epsilon \to 0$.

Theorem 1 *Assume that $v_0^\epsilon(p)$ is bounded uniformly*

$$C^{-1} \le v_0^\epsilon\left(p, \frac{p}{\epsilon}\right) \le D.$$

Denote by $F(t,T)$ the solution to $S_t + f(S)_T = 0$. The solution $\tilde{S}$ of Eq. 12 converges to S^ϵ (assuming initial conditions that don't depend on the fast scale) at a rate given by

$$\|S^\epsilon - \tilde{S}\|_\infty \le G\epsilon,$$

when F remains Lipschitz for all time, and

$$\|S^\epsilon - \tilde{S}\|_n \le G\epsilon^{1/n},$$

when F develops at most a finite number of discontinuities.

The proof of this theorem is provided in the Appendix (see also [23]). We remark that T, which is time-of-flight, is used as an independent variable. We briefly show the results of a numerical experiment to demonstrate the estimate of Theorem 1 for a discontinuous solution. We consider a nonlinear flux $f(S)$ with $\mu_o = \mu_w = 1$, $T_{final} = 0.1$, $v = 1 - 20p\sin\left(10\pi\frac{1}{p+0.1}\right) + 20sin\left(5\frac{\pi}{2}\right)$. Note that we only solve the hyperbolic equation, and Riemann initial condition is considered. To find the rate of convergence of $\tilde{S}$ to S^ϵ, we have to use a grid that resolves the velocity and the shock so that numerical error, especially the numerical diffusion near the shock, does not mask the upscaling error. We use a grid of 4,096 cells for both upscaled and fine computation to avoid the discretization errors as much as possible. At the same time, the velocity must vary enough in the cells so that the upscaling error is large. The top row of Table 1 shows the number of coarse grid blocks. To avoid numerical diffusion, we use a small final time. The upscaling errors are shown in Table 1. The L_∞ norm shows that, in all experiments with less than 64 coarse cells, the numerical diffusion was not significant. The convergence rate seems to be slightly larger than 1, which is consistent with Theorem 1.

The homogenized operator given by Eq. 12 still contains variation of order ϵ through the fast variable $\frac{\psi}{\epsilon}$; however, there, it does not contain any derivatives in that variable. Its dependence on $\frac{\psi}{\epsilon}$ is only parametric. We can homogenize the dependence of the partially homogenized operator on $\frac{\psi}{\epsilon}$ and arrive at a homogenized

Table 1 Numerical demonstration of Theorem 1

	2	4	8	16	32	64	128
L_1	0.0432	0.0124	0.0063	0.0049	0.0022	6.62×10^{-4}	1.41×10^{-4}
L_∞	0.670	0.664	0.663	0.665	0.653	0.61	0.096

operator that is independent of the small scale. In the latter case, we will only obtain weak convergence of the partially homogenized solution. When we homogenized along the streamlines, the resulting equation was of hyperbolic type, like the original equation. In a seminal and celebrated paper, Tartar [24] showed that homogenization across streamlines leads to transport with the average velocity plus a time-dependent diffusion term, referred to as macrodispersion, a physical phenomenon that was not present in the original fine equation. In particular, if the velocity field does not depend on p inside the cells, that is, $\tilde{v}(\psi, \frac{\psi}{\epsilon})$, then the homogenized solution, $\overline{\tilde{S}}$ (weak* limit of $\tilde{S}$, which will be denoted by $\overline{S}$), satisfies

$$\overline{S}_t + \overline{\tilde{v}}_0 \overline{S}_p = \int_0^t \int \overline{S}_{pp}(p - \lambda(t-\tau), \psi, \tau) d\mu_{\frac{\psi}{\epsilon}}(\lambda) d\tau. \tag{15}$$

Here, $dv_{\frac{\psi}{\epsilon}}$ the Young measure associated with the sequence $\tilde{v}_0(\psi, \cdot)$ and $d\mu_{\frac{\psi}{\epsilon}}$ is a Young measure that satisfies

$$\left(\int \frac{dv_{\frac{\psi}{\epsilon}}(\lambda)}{\frac{s}{2\pi i q} + \lambda} \right)^{-1} = \frac{s}{2\pi i q} + \overline{\tilde{v}}_0 - \int \frac{d\mu_{\frac{\psi}{\epsilon}}(\lambda)}{\frac{s}{2\pi i q} + \lambda}.$$

We have denoted by $\overline{\tilde{v}}_0$ the weak limit of the velocity. This equation has no dependence on the small scale, and we consider it to be the full homogenization of the fine saturation equation. Efendiev and Popov [14] have extended this method for the Riemann problem in the case of nonlinear flux. Note that the homogenization across streamlines provides a weak limit of partially homogenized solution. Because the original solution S^ϵ strongly converges to partially homogenized solution for each ψ, it can be easily shown that $S^\epsilon \to \overline{S}$ weakly. We omit this proof here.

In numerical simulations, it is difficult to use Eq. 15 as a homogenized operator, and often, a second-order approximation of this equation is used. These approximate equations can also be derived using perturbation analysis. In particular, using the higher moments of the saturation and the velocity, one can model the macrodispersion. In the context of two-phase flow, this idea was introduced by Efendiev et al. [12, 13]. In our case, the computation of the macrodispersion is much simpler because the transport equations have been already averaged along the streamlines, and thus, we will be applying the perturbation technique to one-dimensional problem.

We expand $\tilde{S}$, $\tilde{v_0}$ (following [13]) as an average over the cells in the pressure-streamline frame and the corresponding fluctuations

$$\begin{aligned} \tilde{S} &= \overline{S}(p, \psi, t) + S'(p, \psi, t) \\ \tilde{v}_0 &= \overline{\tilde{v}_0}(p, \psi, t) + \tilde{v}_0'(p, \psi, t). \end{aligned} \tag{16}$$

We will derive the homogenized equation for $f(S) = S$. Averaging Eq. 12 with respect to ψ, we find an equation for the mean of the saturation

$$\overline{S}_t + \overline{\tilde{v}_0 S}_p + \overline{\tilde{v}_0' S_p'} = 0.$$

An equation for the fluctuations is obtained by subtracting the above equation from Eq. 12

$$S_t' + (\tilde{v}_0 - \overline{\tilde{v}_0})\, \overline{S}_p + \tilde{v}_0 S_p' - \overline{\tilde{v}_0' S_p'} = 0.$$

Together, the equations for the saturation are

$$\begin{aligned} \overline{S}_t + \overline{\tilde{v}_0 S}_p + \overline{\tilde{v}_0' S_p'} &= 0 \\ S_t' + \tilde{v}_0' \overline{S}_p + \tilde{v}_0 S_p' - \overline{\tilde{v}_0' S_p'} &= 0. \end{aligned} \tag{17}$$

We can consider the second equation to be the auxiliary (cell) problem and the first equation to be the upscaled equation. We remind that the cell problem for a hyperbolic equation is $O(1)$, whereas for an elliptic, it is $O(\epsilon)$. We can obtain an approximate numerical method by solving the cell problem only near the shock region in space time, where the macrodispersion term is largest. In that case, it is best to diagonalize these equations by adding the first to the second one

$$\begin{aligned} \overline{S}_t + \overline{\tilde{v}_0}\, \overline{S}_p &= -\overline{\tilde{v}_0'(\tilde{S}_p - \overline{S}_p)} \\ \tilde{S}_t + \tilde{v}_0 \tilde{S}_p &= 0. \end{aligned}$$

Compared to Eq. 17, it has fewer forcing terms and no cross fluxes, which leads to a numerical method with less numerical diffusion that is easier to implement. In most cases, we can make a better approximation, which is described in the following sections.

4.2 Comparison with the cell problem in the cartesian frame

Before we derive the numerical approximation, we will briefly compare the homogenized equations in flow-based frame with the homogenized equations in a

Cartesian frame obtained recently in Hou et al. [15] and Westhead [26]. The homogenized equations in the Cartesian variables as derived in Hou et al. [15] and Westhead [26] are defined in terms of the average saturation over the coarse blocks $\overline{S}$ and the fluctuations S''. Note that, whereas the fluctuations S' in the pressure-streamline frame depend only on one fast variable, the fluctuations S'' in the Cartesian frame depend on two fast variables. $\mathcal{P}$ is a projection operator onto the average along the streamlines within the cell, which corresponds to the fast variable along the streamlines, and $\mathcal{Q}$ is a projection onto the orthogonal complement, so that any function u can be written as $u = \mathcal{P}(u) + \mathcal{Q}(u)$. With this notation, the homogenized equations are

$$\begin{aligned}
&\overline{S}_t + \overline{\mathbf{v}} \cdot \nabla \overline{S} + \nabla \cdot \overline{\mathbf{v}'' S''} = 0 \\
&S''_t + (\overline{\mathbf{v}} + \mathcal{P}(\mathbf{v}'')) \cdot \nabla S'' + \mathcal{P}(\mathbf{v}'') \cdot \nabla \overline{S} \\
&\quad - \nabla \cdot \overline{\mathbf{v}'' S''} = G\left(x, \frac{x}{\epsilon}, t\right),
\end{aligned} \tag{18}$$

where

$$\begin{aligned}
G\left(x, \frac{x}{\epsilon}, t\right) = (\overline{\mathbf{v}} + \mathcal{P}(\mathbf{v}'')) \cdot \mathcal{Q}(\nabla S'') \\
-\mathcal{P}(\mathcal{Q}(\mathbf{v}'') \cdot \mathcal{Q}(\nabla S'')) + \mathcal{Q}(S'').
\end{aligned}$$

The Cartesian cell problem, which is the equation for the fluctuations in Eq. 18, is a two-dimensional equation along two fast variables. Prior to solving it, one must compute the projections $\mathcal{P}$ and $\mathcal{Q}$, which adds to the complexity of the method and its computational cost. In contrast, the pressure-streamline cell problem in Eq. 17 contains only one fast variable and no projection operator. In some sense, in the pressure-streamline frame, the projection operation, which was carried out by restricting the oscillatory test functions, removes a fast variable and reduces one fast dimension to arrive at the cell problem of Eq. 17. In the Cartesian frame, the projection operation remains in the equations in the form of $\mathcal{P}$ and $\mathcal{Q}$ and the fast variation along the flow is not cleanly removed. This is a strong indication that the pressure-streamline frame reveals the structure of the flow correctly.

4.3 Numerical averaging across streamlines

The derivation in the previous sections contained no approximation. In this section, we follow the same idea as in the derivation to solve the equation for the fluctuations along the characteristics, but with the purpose of deriving an equation on the coarse grid. To achieve this, we will not perform analytical upscaling in the sense of deriving a continuous upscaled equation as in the previous section. We will first discretize the equation with a finite volume method in space and then upscale the resulting equation. Our upscaled equation will therefore be dependent on the numerical scheme.

We use the same definition for the average saturation and the fluctuations as in Eq. 16 and follow the same steps until Eq. 17. We discretize the macrodispersion term in the equation for the average saturation

$$\overline{\tilde{v}'_0 S'_p} = \frac{\overline{\tilde{v}'_0 S'}^{i+1} - \overline{\tilde{v}'_0 S'}^{i}}{\Delta p} + O(\Delta p).$$

A superscript $\cdot^i$ refers to a discrete quantity defined at the center of the conservation cell. Instead of solving the equation for the fluctuations on the fine characteristics as before, which would lead to a fine grid algorithm, we solve it on the coarse characteristics defined by

$$\frac{dP}{dt} = \overline{\tilde{v}_0}, \text{ with } P(p, 0) = p.$$

Compared to the equation that we obtained in the previous section for S', this equation for S' has an extra term, which appears second

$$\begin{aligned}
S' = -\int_0^t \Big(&\tilde{v}'_0(P(p,\tau),\psi)\overline{S}_p(P(p,\tau),\psi,\tau) \\
&+ \tilde{v}'_0(P(p,\tau),\psi) S'_p(P(p,\tau),\psi,\tau) + \overline{\tilde{v}'_0 S'_p}) \Big) d\tau.
\end{aligned}$$

The second term is second-order in fluctuating quantities, and we expect it to be smaller than the first term so we neglect it. As before, we multiply by $\tilde{v}'_0$ and average over ψ to find

$$\overline{\tilde{v}'_0 S'} = -\int_0^t \overline{\tilde{v}'_0 \tilde{v}_0(P(p,\tau),\psi)\overline{S}_p(P(p,\tau),\psi,\tau)} d\tau.$$

In this form at time t, it is necessary to know information about the past saturation in $(0, t)$ to compute the future saturation. Following [13], it can be easily shown that $\overline{S}_p(P(p,\tau),\psi,\tau)$ depends weakly on time, in the sense that the difference between $\overline{S}_p$ and $\overline{S}_p$ is of third-order in fluctuating quantities. Therefore, we can take $\overline{S}_p$ out of the time integral to find

$$\overline{\tilde{v}'_0 S'} = -\int_0^t \overline{\tilde{v}'_0 \tilde{v}'_0(P(p,\tau),\psi)} d\tau \, \overline{S}_p.$$

The term inside the time integral is the covariance of the velocity field along each streamline. The macrodispersion in this form can be computed independent of the past saturation.

The nonlinearity of the flux function introduces an extra source of error in the approximation. We expand $f(\tilde{S})$ near $\overline{S}$ (cf. [12]) and keep only the first term

$$\begin{aligned}\tilde{S} &= \overline{S}(p,\psi,t) + S'(p,\psi,t)\\ \tilde{v}_0 &= \overline{\tilde{v}_0}(p,\psi,t) + \tilde{v}_0'(p,\psi,t)\\ \overline{f(\tilde{S})} &= f(\overline{S}) + f_S(\overline{S})S' + O(S'^2)\\ f(S)_p &= f_S(\overline{S})\overline{S}_p + f(\overline{S})S' + \ldots \end{aligned} \tag{19}$$

This approximation is not accurate near the shock because S' is not small near sharp fronts. The region near the shock is important because the macrodispersion is large. Due to the dependence of the jump in the saturation on the mobility, we expect this approximation to be better for lower oil mobilities. Nevertheless, this approximation works well in practice. For more accuracy, it is also possible to retain more terms in the Taylor expansion. We will show that, in realistic examples, these higher-order terms are not important in our setting.

Using these definitions, we derive the following equations for the average saturation and the fluctuations (see [23] for more details)

$$\overline{S}_t + \overline{\tilde{v}_0} f(\overline{S})_p + \overline{\tilde{v}_0'(f_S(\overline{S})S')_p} = 0 \tag{20}$$

$$S'_t + \tilde{v}_0' f_S(\overline{S})\overline{S}_p + \tilde{v}_0 f_S(\overline{S})S'_p - \overline{\tilde{v}_0' S'_p} = 0. \tag{21}$$

The macrodispersion is discretized as

$$\overline{\tilde{v}_0'(f_S(\overline{S})S')_p} = \frac{\overline{\tilde{v}_0' f_S(\overline{S})S'}^{i+1} - \overline{\tilde{v}_0' f_S(\overline{S})S'}^{i}}{\Delta p} + O(\Delta p).$$

We solve the second equation on the coarse characteristics defined by

$$\frac{dP}{dt} = \overline{\tilde{v}_0} f_S(\overline{S}), \text{ with } P(p,0) = p$$

and form the terms that appear in the macrodispersion

$$\overline{\tilde{v}_0' f_S(\overline{S})S'} = -\int_0^t \overline{\tilde{v}_0' f_S(\overline{S})\tilde{v}_0'(P(p,\tau),\psi) f_S(\overline{S}(P(p,\tau),\psi,\tau))\overline{S}_p(P(p,\tau),\psi,\tau)}d\tau.$$

As before, we have dropped terms that are second-order in fluctuating quantities. It can be shown (see [23]) that $f_S(\overline{S}(P(p,\tau),\psi,\tau))\overline{S}_p(P(p,\tau),\psi,\tau)$ does not vary significantly along the streamlines, and it can be taken out of the integration in time:

$$\overline{\tilde{v}_0' f_S(\overline{S})S'} = -\int_0^t \overline{\tilde{v}_0'\tilde{v}_0'(P(p,\tau),\psi)}d\tau f_S(\overline{S})^2\overline{S}_p. \tag{22}$$

This expression is similar to the one obtained in the linear case; however, the macrodispersion depends on the past saturation through the equation for the coarse characteristics.

Even though the macrodispersion depends on the past saturation, it is possible to compute it incrementally, as it is done in Efendiev and Durlofsky [12]. Given its value $D(t)$ at time t, we compute the values at $t+\Delta t$ using the macrodispersion at the previous time

$$D(t+\Delta t) = \int_0^{t+\Delta t} \ldots d\tau = \int_0^t \ldots d\tau + \int_t^{t+\Delta t} \ldots d\tau.$$

This is possible because, in the derivation for the approximate expression for the macrodispersion, we took the terms that depend on $S(\tau)$ outside the time integration. The integrand, the average covariance of the velocity field along the streamlines, needs to be computed only once at the beginning. Then, updating the macrodispersion takes $O(n^2)$ computations, as many as it takes to update $\overline{S}$.

5 Multiscale finite element methods for upscaling of pressure equation

The multiscale finite element framework will be used for upscaling of the pressure equation. We will choose a finite volume element method as a global solver. The proposed method is similar to an earlier introduced multiscale finite volume method in Jenny et al. [19, 20]. Let $\mathcal{K}^h$ denote the collection of coarse elements/rectangles K. Consider a coarse element K, and let $\boldsymbol{\xi}_K$ be its center. The element K is divided into four rectangles of equal area by connecting $\boldsymbol{\xi}_K$ to the midpoints of the element's edges. We denote these quadrilaterals by $K_{\boldsymbol{\xi}}$, where $\boldsymbol{\xi} \in Z_h(K)$ are the vertices of K. Also, we denote $Z_h = \bigcup_K Z_h(K)$ and $Z_h^0 \subset Z_h$ the vertices that do not lie on the Dirichlet boundary of Ω. The control volume $V_{\boldsymbol{\xi}}$ is defined as the union of the quadrilaterals $K_{\boldsymbol{\xi}}$ sharing the vertex $\boldsymbol{\xi}$.

The key idea of the method is the construction of basis functions on the coarse grids, such that these basis functions capture the small-scale information on each of these coarse grids. The basis functions are constructed from the solution of the leading order

homogeneous elliptic equation on each coarse element with some specified boundary conditions. Thus, if we consider a coarse element K that has d vertices, the local basis functions $\phi_i, i = 1, \cdots, d$ are set to satisfy the following elliptic problem:

$$-\nabla \cdot (\mathbf{k} \cdot \nabla \phi_i) = 0 \quad \text{in } K, \quad \phi_i = g_i \quad \text{on } \partial K, \tag{23}$$

for some function g_i defined on the boundary of the coarse element K. In previous findings, the function g_i for each i is chosen to vary linearly along ∂K or to be the solution of the local one-dimensional problems [19] or the solution of the problem in a slightly larger domain is chosen to define the boundary conditions [16]. We will be using linear boundary conditions and require $\phi_i(\mathbf{x}_j) = \delta_{ij}$. Finally, a nodal basis function associated with the vertex $\mathbf{x}_i$ in the domain Ω is constructed from the combination of the local basis functions that share this $\mathbf{x}_i$ and zero elsewhere.

Next, we denote by V^h the space of our approximate pressure solution, which is spanned by the basis functions $\{\phi_j\}_{\mathbf{x}_j \in Z_h^0}$. A statement of mass conservation on a coarse-control volume $V_{\mathbf{x}}$ is formed from (2), where now the approximate solution is written as a linear combination of the basis functions. Assembly of this conservation statement for all control volumes would give the corresponding linear system equations that can be solved accordingly. To be specific, the problem now is to seek $P^h \in V^h$ with $P^h = \sum_{\mathbf{x}_j \in Z_h^0} P_j \phi_j$ such that

$$\int_{\partial V_\xi} \lambda(S) \mathbf{k} \cdot \nabla P^h \cdot \mathbf{n} \, dl = 0, \tag{24}$$

for every control volume $V_\xi \subset \Omega$. Here, $\mathbf{n}$ defines the normal vector on the boundary of the control volume, ∂V_ξ, and S is the fine-scale saturation field at this point.

In the previous studies [1, 7, 11], it was found that the use of global information can improve the multiscale finite element method. In particular, the solution of the pressure equation at initial time is used to construct the boundary conditions for the basis functions. It is interesting to note that the multiscale finite element methods that employ a limited global information reduce to standard multiscale finite element methods in a flow-based coordinate system. This can be verified directly, and the reason behind it is that we have already employed a limited global information in a flow-based coordinate system.

6 Numerical results

In this section, we first show representative simulation results for $\lambda(S) = 1$ for flux functions $f(S) = S$ and nonlinear $f(S)$ with viscosity ratio $\mu_o/\mu_w = 5$. For such a setting, the pressure and saturation equations are decoupled and we can investigate the accuracy of saturation upscaling independently from the pressure upscaling. We note that this decoupling of the pressure and saturation equations is artificial. At the end of the section, we will present numerical results for two-phase flow with variable $\lambda(S)$. We consider two types of permeability fields. The first type includes a permeability field generated using two-point geostatistics with correlation lengths $l_x = 0.3$, $l_z = 0.03$, and $\sigma^2 = 1.5$ (see Fig. 1, left). The second type corresponds to a channelized system, and we consider two examples. The first example (middle figure of Fig. 1) is a synthetic channelized reservoir generated using both multipoint geostatistics (for the channels) and two-point geostatistics (for permeability distribution within each facies). The second channelized system is one of the layers of the benchmark test (representing the North Sea reservoir), the Society of Petroleum Engineers comparative project [9] (upper Ness layers). These permeability fields are highly heterogeneous, channelized, and difficult to upscale. Because the permeability fields are

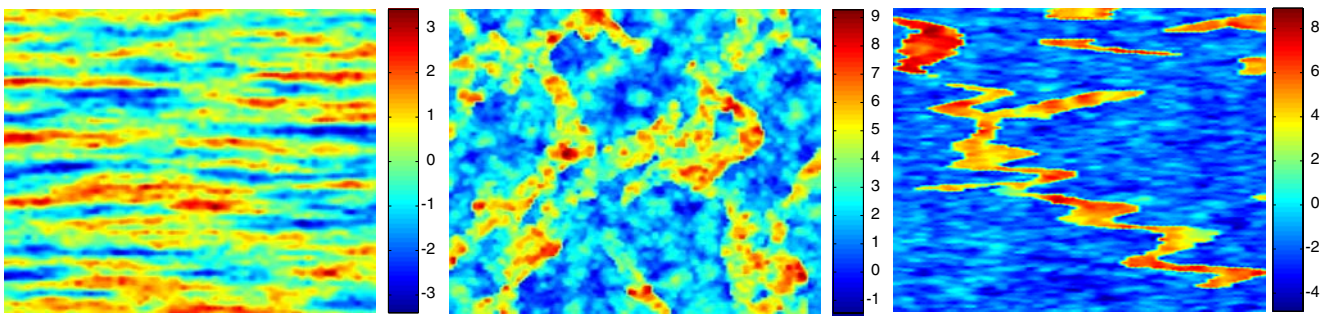

Fig. 1 Permeability fields used in the simulations. *Left*, permeability field with exponential variogram; *middle*, synthetic channelized permeability field; *right*, layer 36 of the Society of Petroleum Engineers comparative project [9]

highly heterogeneous, they are refined to 400×400 to obtain accurate comparisons.

Simulation results will be presented for saturation snapshots and the oil cut as a function of pore volume injected (PVI). Note that the oil cut is also referred to as the fractional flow of oil. The oil cut (or fractional flow) is defined as the fraction of oil in the produced fluid and is given by q_o/q_t, where $q_t = q_o + q_w$, with q_o and q_w being the flow rates of oil and water at the production edge of the model. In particular, $q_w = \int_{\partial\Omega^{out}} f(S)\mathbf{v}\cdot\mathbf{n}dl$, $q_t = \int_{\partial\Omega^{out}} \mathbf{v}\cdot\mathbf{n}dl$, and $q_o = q_t - q_w$, where $\partial\Omega^{out}$ is the outer flow boundary. We will use the notation Q for total flow q_t and F for fractional flow q_o/q_t in numerical results. PVI, defined as $PVI = \frac{1}{V_p}\int_0^t q_t(\tau)d\tau$, with V_p being the total pore volume of the system, provides a dimensionless time for the displacement.

When using multiscale finite element methods for two-phase flow, one can update the basis functions near the sharp fronts. Indeed, sharp fronts modify the local heterogeneities, and this can be taken into account by resolving the local equations, Eq. 23, for basis functions. If the saturation is smooth in the coarse block, it can be approximated by its average in Eq. 23, and consequently, the basis functions do not need to be updated. It can be shown that this approximation yields first-order errors (in terms of coarse mesh size). In our simulations, we have found only a slight improvement when the basis functions are updated; thus, the numerical results for the MsFEM presented in this paper do not include the basis function update near the sharp fronts. Because a pressure-streamline coordinate system is used, the boundary conditions are given by $P = 1$, $S = 1$ along the $p = 1$ edge and $P = 0$ along the $p = 0$ edge, and no flow boundary condition on the rest of the boundaries.

For the upscaled saturation equation, which is a convection–diffusion equation, we need to observe an extra Courant–Friedrichs–Lewy (CFL)-like condition to obtain a stable numerical scheme $\Delta t \leq \frac{\Delta p^2}{2\nu}$, where ν is the diffusivity. In our case, the diffusivity is

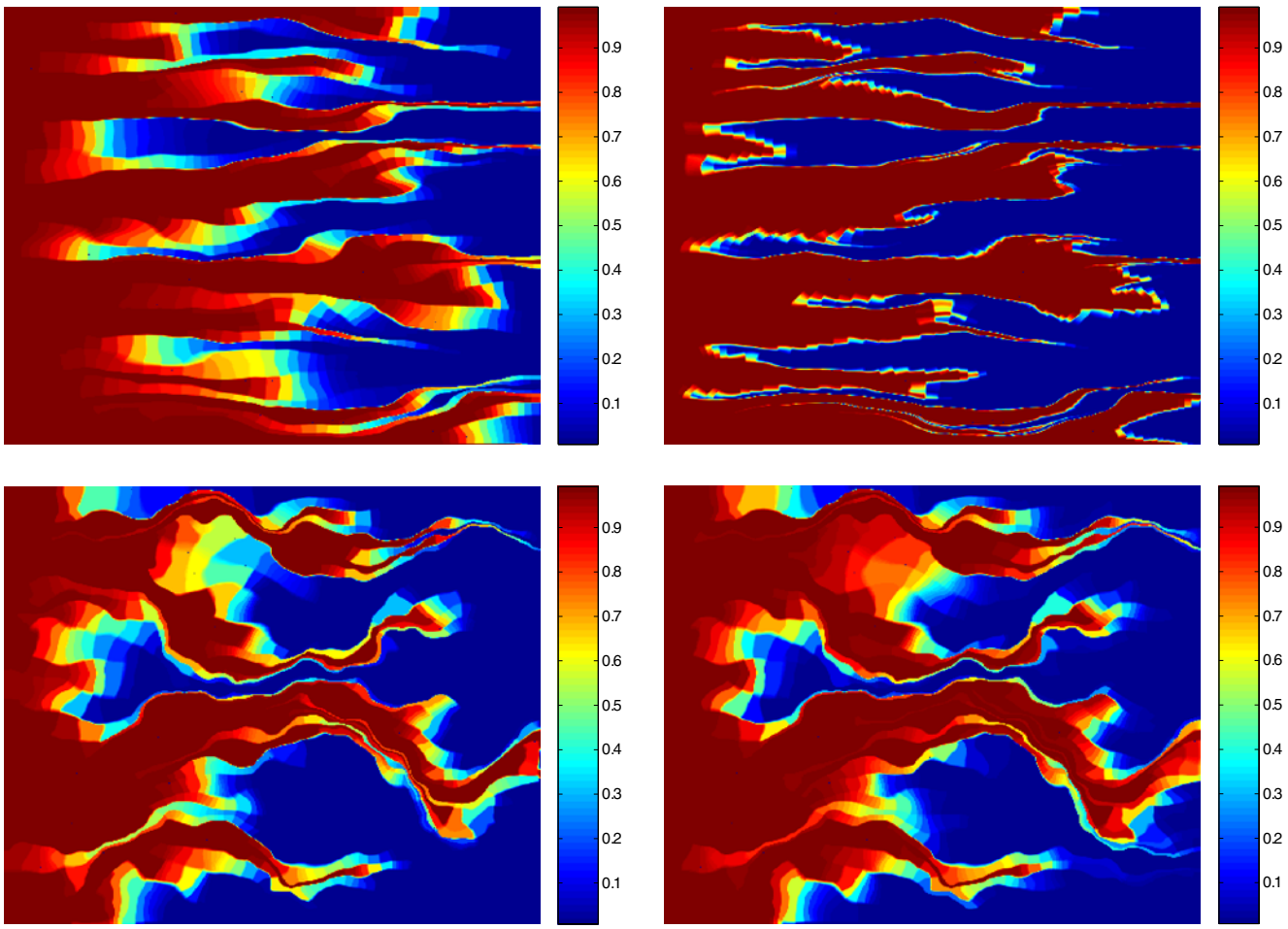

Fig. 2 Saturation snapshots for variogram based permeability field (*top*) and synthetic channelized permeability field (*bottom*). Linear flux is used. The *left figures* represent the upscaled saturation plots, and the *right figures* represent the fine-scale saturation plots

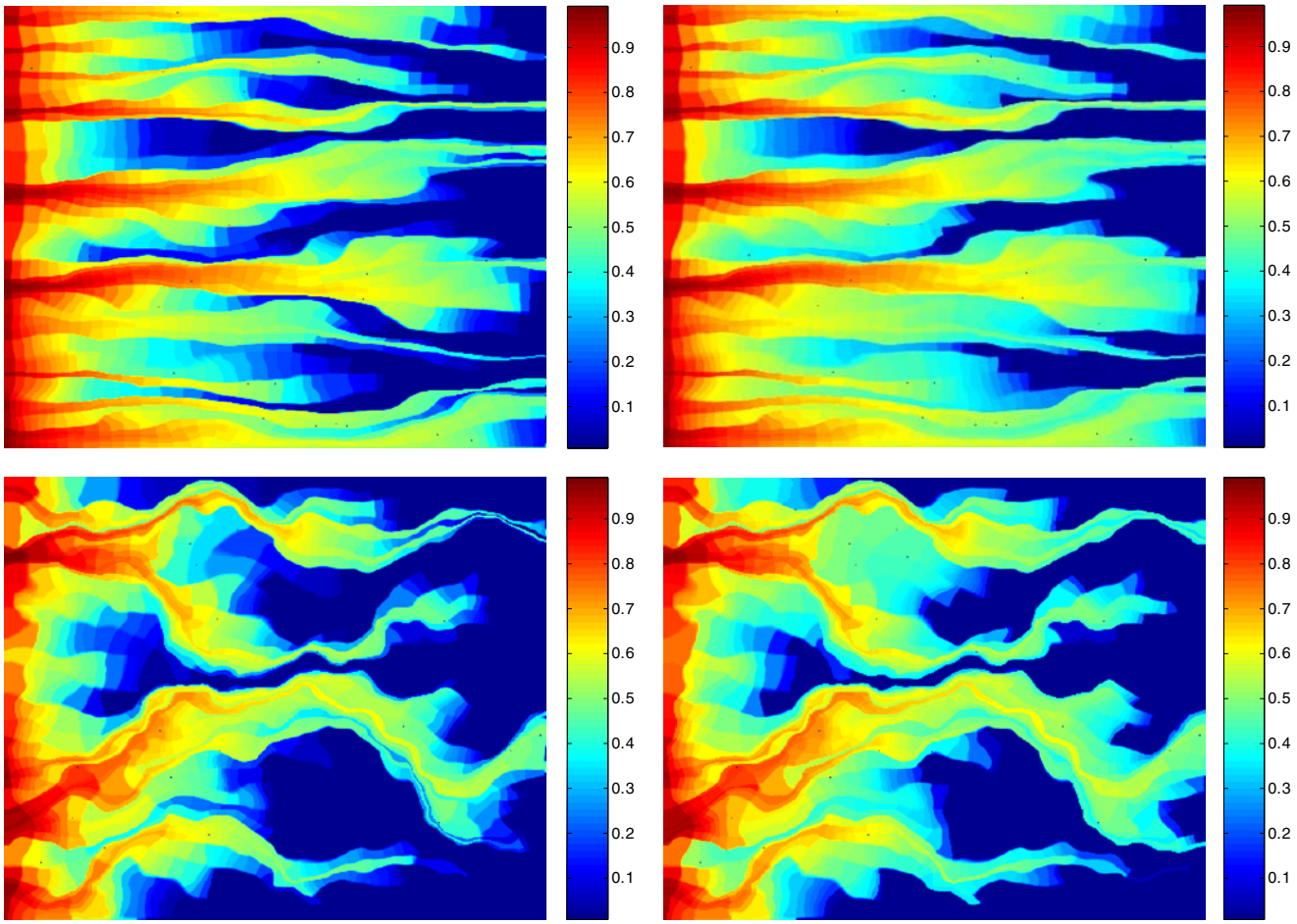

Fig. 3 Saturation snapshots for variogram based permeability field (*top*) and synthetic channelized permeability field (*bottom*). Nonlinear flux is used. The *left figures* represent the upscaled saturation plots, and the *right figures* represent the fine-scale saturation plots

$\int_{cell}\int_0^t \tilde{v}_0'(p(\tau),\psi)\tilde{v}_0'(p,\psi)d\tau d\psi$. If the macrodispersion is large, this can be a very restrictive condition. To remedy this, we used an implicit discretization for the macrodispersion. This is straightforward because the problem is one-dimensional. The resulting system was solved by a tridiagonal solver very fast. Because the order of the highest derivative in the equation has increased, we require extra boundary conditions. For the computation of the macrodispersion term, we impose no flux on both boundaries of the domain.

In the upscaled algorithm, a moving mesh is used to concentrate the points of computation near the sharp front. Because the saturation equation is one-dimensional in the pressure-streamline coordinates, the implementation of the moving mesh is straightforward and efficient. For the details, we refer to Strinopoulos [23]. We compare the saturation right before the breakthrough time so that the shock front is largest. For this comparison, we also average the fine saturation over the coarse blocks because the upscaled model is defined

Table 2 Upscaling error for permeability generated using two-point geostatistics

	25×25	50×50	100×100	200×200
Linear flux				
L_1 error of $\tilde{S}$	0.0021	6.57×10^{-4}	2.15×10^{-4}	8.75×10^{-5}
L_1 error of $\overline{S}$ with macrodispersion	0.115	0.0696	0.0364	0.0135
L_1 error of $\overline{S}$ fine without macrodispersion	0.1843	0.0997	0.0505	0.0191
Nonlinear flux				
L_1 error of $\tilde{S}$	0.0023	8.05×10^{-4}	2.89×10^{-4}	1.29×10^{-4}
L_1 error of $\overline{S}$ with macrodispersion	0.116	0.0665	0.0433	0.0177
L_1 error of $\overline{S}$ fine without macrodispersion	0.151	0.0805	0.0432	0.0186

Table 3 Upscaling error for synthetic channelized permeability field

	25×25	50×50	100×100	200×200
Linear flux				
L_1 error of $\tilde{S}$	0.0222	0.0171	0.0122	0.0053
L_1 error of $\overline{S}$ with macrodispersion	0.0819	0.0534	0.0333	0.0178
L_1 error of $\overline{S}$ fine without macrodispersion	0.123	0.0834	0.0486	0.0209
Nonlinear flux				
L_1 error of $\tilde{S}$	0.0147	0.0105	0.0075	0.0040
L_1 error of $\overline{S}$ with macrodispersion	0.0842	0.0658	0.0371	0.0207
L_1 error of $\overline{S}$ fine without macrodispersion	0.119	0.0744	0.0424	0.0214

Table 4 Upscaling error for SPE10, layer 36

	25×25	50×50	100×100	200×200
Linear flux				
L_1 error of $\tilde{S}$	0.0128	0.0093	0.0072	0.0042
L_1 error of $\overline{S}$ with macrodispersion	0.0554	0.0435	0.0307	0.0176
L_1 error of $\overline{S}$ fine without macrodispersion	0.123	0.0798	0.0484	0.0258
Nonlinear flux				
L_1 error of $\tilde{S}$	0.0089	0.0064	0.0054	0.0033
L_1 error of $\overline{S}$ with macrodispersion	0.0743	0.0538	0.0348	0.0189
L_1 error of $\overline{S}$ fine without macrodispersion	0.0924	0.0602	0.0395	0.0202

Table 5 Total error for permeability field generated using two-point geostatistics

	25×25	50×50	100×100	200×200
Linear flux				
L_1 upscaling error of $\tilde{S}$	0.0021	6.57×10^{-4}	2.15×10^{-4}	8.75×10^{-5}
L_1 error of $\tilde{S}$ computed on coarse grid	0.0185	0.0062	0.0019	0.0015
L_1 upscaling error of $\overline{S}$	0.115	0.0696	0.0364	0.0135
L_1 error of $\overline{S}$ computed on coarse grid	0.139	0.0779	0.0390	0.0144
Nonlinear flux				
L_1 upscaling error of $\tilde{S}$	0.0023	8.05×10^{-4}	2.89×10^{-4}	1.29×10^{-4}
L_1 error of $\tilde{S}$ computed on coarse grid	0.0268	0.0099	0.0027	9.38×10^{-4}
L_1 upscaling error of $\overline{S}$	0.116	0.0665	0.0433	0.0177
L_1 error of $\overline{S}$ computed on coarse grid	0.146	0.0797	0.0461	0.0184

Table 6 Total error for synthetic channelized permeability field

	25×25	50×50	100×100	200×200
Linear flux				
L_1 upscaling error of $\tilde{S}$	0.0222	0.0171	0.0122	0.0053
L_1 error of $\tilde{S}$ computed on coarse grid	0.0326	0.0161	0.0107	0.0113
L_1 upscaling error of $\overline{S}$	0.0819	0.0534	0.0333	0.0178
L_1 error of $\overline{S}$ computed on coarse grid	0.135	0.0849	0.0477	0.0274
Nonlinear flux				
L_1 upscaling error of $\tilde{S}$	0.0147	0.0105	0.0075	0.0040
L_1 error of $\tilde{S}$ computed on coarse grid	0.0494	0.0295	0.0150	0.0130
L_1 upscaling error of $\overline{S}$	0.0842	0.0658	0.0371	0.0207
L_1 error of $\overline{S}$ computed on coarse grid	0.17	0.11	0.0541	0.0303

Table 7 Total error for SPE10 layer 36

	25 × 25	50 × 50	100 × 100	200 × 200
Linear flux				
L_1 upscaling error of $\tilde{S}$	0.0128	0.0093	0.0072	0.0042
L_1 error of $\tilde{S}$ computed on coarse grid	0.023	0.0095	0.0069	0.0052
L_1 upscaling error of $\overline{S}$	0.0554	0.0435	0.0307	0.0176
L_1 error of $\overline{S}$ computed on coarse grid	0.0683	0.052	0.0361	0.0205
Nonlinear flux				
L_1 upscaling error of $\tilde{S}$	0.0089	0.0064	0.0054	0.0033
L_1 error of $\tilde{S}$ computed on coarse grid	0.0338	0.0148	0.0074	0.0037
L_1 upscaling error of $\overline{S}$	0.0743	0.0538	0.0348	0.0189
L_1 error of $\overline{S}$ computed on coarse grid	0.115	0.0720	0.0406	0.0204

on a coarser grid. In Figs. 2 and 3, we plot the saturation for linear and nonlinear (with $\mu_o/\mu_w = 5$) $f(S)$. We remind that $\lambda(S) = 1$ in these simulations. As we see in both cases, we have very accurate representation of the saturation profile.

We proceed with a quantitative description of the error. We will distinguish between two sources of errors. We will refer to the difference between the upscaled and the fine-scale solution as the upscaling or modeling error. In this case, the upscaled equations are solved on the fine grid to avoid the discretization errors on the coarse grid. We note that the discretization errors, such as the ones associated with a numerical diffusion, can be very large on relatively coarse grids. We will refer to the difference between the fine-scale solution and the solution of the upscaled equation on the coarse grid as the total error. In this case, the upscaled equations are solved on the coarse grid and the total error includes both the upscaling error and the discretization error on the coarse grid. To compute the upscaling error, we compare the upscaled solution computed on a 400×400 grid with the fine-scale saturation computed on the 400×400 grid and averaged over the coarse grid. The errors are computed in the p, ψ frame and are relative errors. We display the upscaling error against the number of coarse cells in Tables 2, 3, and 4. Linear flux and nonlinear ($\mu_o/\mu_w = 5$) flux cases are considered with $\lambda(S) = 1$. In these tables, $\tilde{S}$ refers to the solution upscaled along streamlines (see Eq. 12) and $\overline{S}$ refers to the solution upscaled both along and across the streamlines (see Eq. 21). We see from this table that upscaling using macrodispersion reduces the upscaling errors. Note that the effects of macrodispersion are more significant in the case of linear flux when the jump discontinuity in the saturation profile is larger. We remark that the macrodispersion errors become less significant as the coarse mesh size decreases. Because the sharp fronts are resolved in our numerical simulations, the macrodispersion represents the fluctuations of the solution away from these fronts. The effects of these fluctuations decrease as the coarse mesh becomes smaller.

In Tables 5, 6, and 7, we show the total error, that is, the modeling and discretization error, for the cases considered in Tables 2, 3, and 4. We again remind that $\tilde{S}$ is the solution upscaled along streamlines (see Eq. 12), $\overline{S}$ is the solution upscaled both along and across the streamlines (see Eq. 21). The first and third rows in these tables are the errors computed on the fine grid, while the second and fourth rows represent the errors computed on the coarse grid. First, we note that the total errors are much smaller when the upscaling is only performed along the streamlines. It is interesting that the convergence of $\tilde{S}$ to S is observed even though the upscaling error is larger than the numerical error of the fine solution. The reason is that the location of the

Table 8 Computational cost

	Fine $x.y$	Fine p, ψ	$\tilde{S}$	$\overline{S}$
Layered, linear flux	5648	257	9	1
Layered, nonlinear flux	14543	945	28	4
Percolation, linear flux	8812	552	12	1
Percolation, nonlinear flux	23466	579	12	1
SPE10 36, linear flux	40586	1835	34	2
SPE10 36, nonlinear flux	118364	7644	25	2

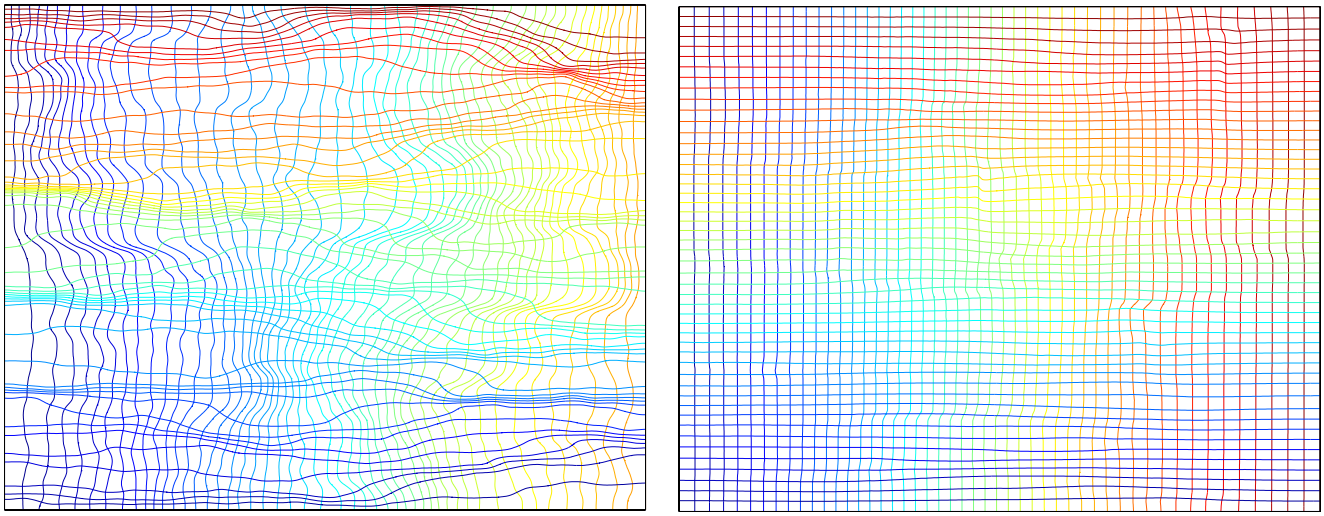

Fig. 4 *Left*: pressure and streamline function at time $t = 0.4$ in Cartesian frame. *Right*: pressure and streamline function at time $t = 0.4$ in initial pressure-streamline frame

moving mesh points was selected so that the points are as dense near the shock as the fine solution using the parameter h_{min}. This was done to observe the upscaling error clearly and also to have similar CFL constraints on the time step, which allows a clean comparison of computational times. We compare the require CPU times in Table 8. We note that it took 26 units of time to interpolate one quantity from the Cartesian to the pressure-streamline frame. The upscaled solutions were computed on a 25×25 grid, and the fine solution was computed on a 400×400 grid, so we expect the $\overline{S}$ computations to be 256 times faster or more. The extra gain comes from a less restrictive CFL condition because we use an averaged velocity. The computations in the Cartesian frame are much slower.

The application of the proposed method to two-phase immiscible flow can be performed using the implicit pressure and explicit saturation (IMPES) framework. This procedure consists of computing the velocity and then using the velocity field in updating the saturation field. When updating the saturation field, we consider the velocity field to be time-independent, and we can use our upscaling procedure at each IMPES time step. First, we note that, in the proposed method, the mapping is done between the current pressure-streamline and initial pressure-streamline. This mapping is nearly the identity for lower oil mobilities. In Fig. 4, we plot the level sets of the pressure and stream function at time $t = 0.4$ in a Cartesian coordinate system (left plot) and in the coordinate system of the

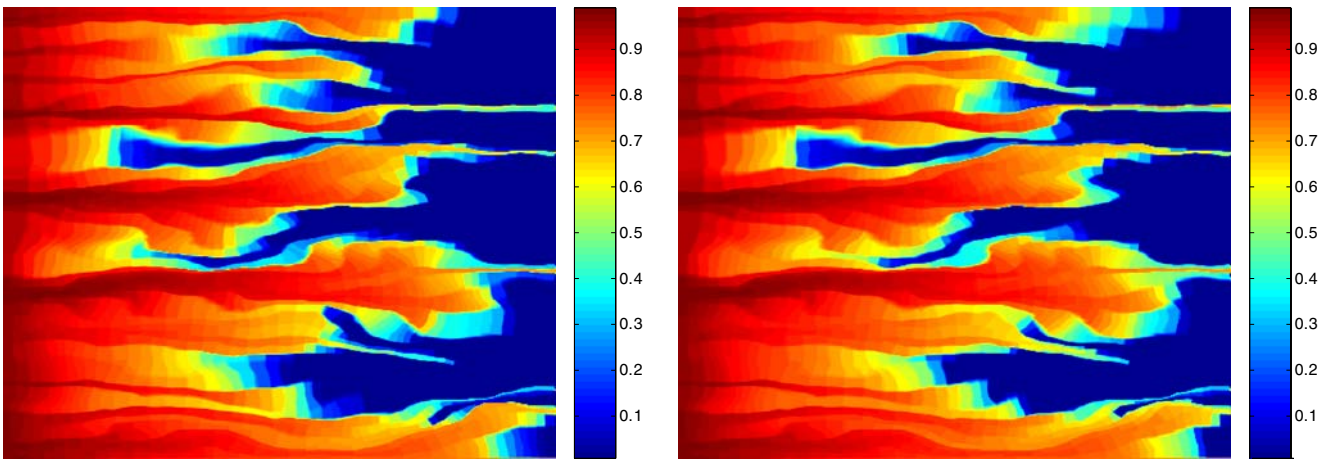

Fig. 5 *Left*: Saturation plot obtained using coarse-scale model. *Right*: The fine-scale saturation plot. Both plots are on coarse grid. Variogram based permeability field is used. $\mu_o/\mu_w = 5$

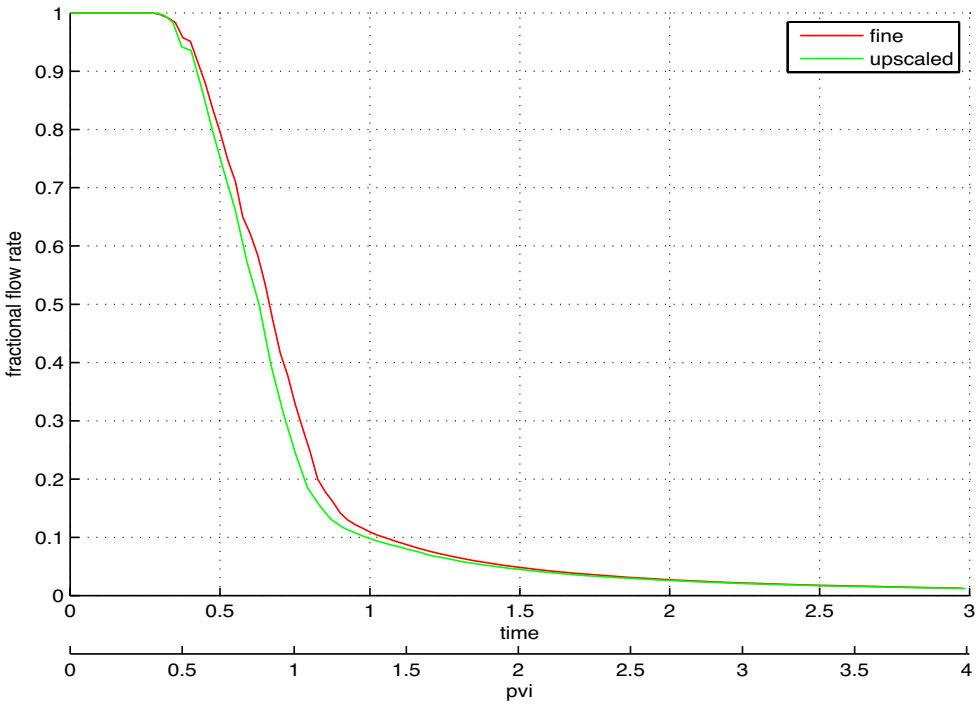

Fig. 6 Comparison of fractional flow for coarse- and fine-scale models. Variogram-based permeability field is used. $\mu_o/\mu_w = 5$

initial pressure and streamline (right plot). Clearly, the level sets are much smoother in initial pressure-streamline frame compared to Cartesian frame. This also explains the observed convergence of upscaling methods as we refined the coarse grid. In Fig. 5, we plot the saturation snapshots right before the breakthrough. In Fig. 6, the fractional flow is plotted. Again, the moving mesh algorithm is used to track the front separately. The convergence table is presented in Table 9. We see from this table that the errors decreases as first order, which indicates that the pressure and saturation are smooth functions of initial pressure and streamline.

Table 9 Convergence of the upscaling method for two-phase flow for variogram based permeability field

	50×50	100×100	200×200
With $\tilde{S}$			
L_2 pressure error at $t = \frac{3T_{final}}{4}$	0.0014	0.0007	0.0004
L_2 velocity error at $t = \frac{3T_{final}}{4}$	0.0235	0.0137	0.0072
L_1 saturation error $t = T_{final}$	0.0105	0.0052	0.0027
With $\overline{S}$			
L_2 pressure error at $t = \frac{3T_{final}}{4}$	0.0046	0.0021	0.0008
L_2 velocity error at $t = \frac{3T_{final}}{4}$	0.0530	0.0335	0.0246
L_1 saturation error $t = T_{final}$	0.0546	0.0294	0.0134

7 Conclusions

In this paper, multiscale methods for two-phase immiscible flow using flow-based coordinate system are considered. In particular, the upscaling of a convection-dominated transport equation is discussed. The flow-based coordinate system allows us to simplify the scale interaction and obtain an upscaled model for transport. Furthermore, this upscaled model is used to design a coarse-scale algorithm for two-phase flow. In our numerical methods, the shock front of the upscaled equation was resolved using a moving mesh. Numerical results show that one can achieve high accuracy using the proposed algorithms. The proposed methods are efficient when the solution is smooth in a new coordinate system (perhaps with the exception of some sharp moving fronts). However, if, under changing source terms or boundary conditions, the solution dramatically changes and no longer remains smooth, then one may need to introduce another coordinate system for accurate coarse-scale simulations.

Though the results presented in the paper are encouraging, there are possible extensions that are currently under investigation. The extension to three dimensions does not seem to be difficult. However, it fails when the coordinate transformation becomes degenerate. We conjecture (see [23]) that, for most permeability fields, the regions of the flow where this

occurs do not carry much fluid. It should then be possible to regularize the transformation and apply this method with only a small numerical error. Another direction of future research is the development of fast and accurate algorithms that perform interpolation from the Cartesian to pressure-streamline grid. In particular, our interest is in the development of such algorithms using coarse-scale information similar to multiscale finite element methods. The latter will speed-up the interpolation computations and make the method more desirable for multiphase flow and transport computations.

Acknowledgements We would like to thank Dr. Victor Ginting for providing us with the multiscale finite volume code. We would like also to thank Dr. Yuguang Chen for providing us with the synthetic channelized permeability fields and the reviewers for their valuable comments. This research is supported by DOE grant DE-FG02-06ER25727. T.Y.H. would like also to acknowledge partial support from the NSF Information Technology Research grant ACI-0204932 and the NSF Focused Research Groups grant DMS-0353838.

Appendix

Proof of Theorem 1

First, we note that the velocity bound implies that $\tilde{C}^{-1} \leq \tilde{v}_0(p) \leq \tilde{D}$, uniformly. We transform the equations for S^ϵ Eq. 11 and $\tilde{S}$ Eq. 12 to the time-of-flight variable defined by

$$\frac{dT^\epsilon}{dp} = \frac{1}{v_0^\epsilon(p,\psi)} \text{ for } S^\epsilon \text{ and } \frac{d\tilde{T}}{dp} = \frac{1}{\tilde{v}\left(p,\psi,\frac{\psi}{\epsilon}\right)} \text{ for } \tilde{S}.$$
$$T^\epsilon(0) = 0 \qquad \tilde{T}(0) = 0$$

Both equations reduce to

$$S_t + f(S)_T = 0.$$

The solution to this equation is $F(t, T)$. Because the initial condition does not depend on ϵ, neither does F. Then, $S = F(t, T^\epsilon(P, \Psi))$, $\tilde{S} = F(t, \tilde{T}(P, \Psi))$. Using these expressions for the saturation, we can obtain the desired estimates by following the same steps as in the linear case. When F remains Lipschitz for all times we can easily obtain a pointwise estimate in terms of the Lipschitz constant M $\|S^\epsilon - \tilde{S}\|_\infty = \|F(t, T^\epsilon) - F(t, \tilde{T})\|_\infty \leq M\|T^\epsilon - \tilde{T}\|_\infty \leq G\epsilon$. Otherwise, we will need the time-of-flight bound that we derived for the linear flux that reduces here to

$$|T^\epsilon(P) - \tilde{T}(P)| \leq 2C\epsilon. \tag{25}$$

We will divide the domain in regions where F is Lipschitz with constant M in the second variable, denoted by A_2, and shock regions, denoted by A_1, and estimate the difference of S^ϵ and $\tilde{S}$ in each region separately. To fix the notation, let there be n discontinuities in $F(t, \cdot)$ of magnitude less than ΔF, which does not have to be small, at $\{T = T_i\}_{i=1,\ldots,n}$. We will denote the thin strips of width $2C\epsilon$ around the discontinuities with A_1

$$A_1 = \{T \text{ such that } |T - T_i| \leq 2C\epsilon, \text{ for some } i = 1, \ldots, n\}$$

and with A_2 its complement. We selected the width of the strip based on Eq. 25, so that for any point P, if $T^\epsilon(P) \notin A_1$, then $T^\epsilon(P)$ and $\tilde{T}(P)$ are on the same side of any jump T_i. When $T^\epsilon(P) \in A_2$, F is Lipschitz in the region between T^ϵ and $\tilde{T}$, and we can show

$$\begin{aligned}\int_{A_2}(S^\epsilon - \tilde{S})^2 dp d\psi &= \int_{A_2}(F(t, T^\epsilon) - F(t, \tilde{T}))^2 dp d\psi \\ &\leq M^2\|T^\epsilon - \tilde{T}\|_\infty^2 |T^\epsilon(A_2)^{-1}| \\ &\leq N^2\epsilon^2 |T^\epsilon(A_2)^{-1}|,\end{aligned}$$

where we used the time-of-flight bound Eq. 25. By $|T^\epsilon(A_2)^{-1}|$, we denoted the image of A_2 under the inverse of $T^\epsilon(P)$. Inside the strip A_1, even though S^ϵ and $\tilde{S}$ differ by an $O(1)$ quantity, we can use the smallness of the area of the strip to make the L_2 norm of their difference small

$$\begin{aligned}\int_{A_1}(S^\epsilon - \tilde{S})^2 dp d\psi &= \int_{A_2}(F(t, T^\epsilon) - F(t, \tilde{T}))^2 dp d\psi \\ &\leq (\Delta S + N\epsilon)^2 |T^\epsilon(A_1)^{-1}| \\ &\leq (\Delta S + N\epsilon)^2 4CDn\epsilon.\end{aligned}$$

We estimated the area $|T^\epsilon(A_1)^{-1}|$ by using the definition of A_1 and the fact that the Jacobian of the transformation $T^\epsilon(P)^{-1}$ is v_0^ϵ and is bounded uniformly in p, ψ. Putting together the two estimates for regions A_1 and A_2, we obtain $\|S^\epsilon - \tilde{S}\|_2 \leq G\epsilon^{1/2}$. Estimates in terms of the other L_p norms follow similarly.

References

1. Aarnes, J.: On the use of a mixed multiscale finite element method for greater flexibility and increased speed or improved accuracy in reservoir simulation. SIAM Multiscale Model. Simul. **2**, 421–439 (2004)
2. Arbogast, T.: Implementation of a locally conservative numerical subgrid upscaling scheme for two-phase Darcy flow. Comput. Geosci. **6**, 453–481 (2002)
3. Babuška, I., Osborn, E.: Generalized finite element methods: their performance and their relation to mixed methods. SIAM J. Numer. Anal. **20**, 510–536 (1983)
4. Babuška, I., Caloz, G., Osborn, E.: Special finite element methods for a class of second order elliptic problems with rough coefficients. SIAM J. Numer. Anal. **31**, 945–981 (1994)
5. Bourgeat, A., Mikelić, A.: Homogenization of two-phase immiscible flows in a one-dimensional porous medium. Asymptot. Anal. **9**, 359–380 (1994)

6. Brezzi, F.: Interacting with the subgrid world. In: Griffiths, D.F., Watson, G.A. (eds.) Numerical Analysis 1999 (Dundee), pp. 69–82. Chapman & Hall/CRC, Boca Raton, FL (2000)
7. Chen, Y., Durlofsky, L.J.: Adaptive coupled local-global upscaling for general flow scenarios in heterogeneous formations. Transp. Porous Media **62**, 157–185 (2006)
8. Chen, Z., Hou, T.Y.: A mixed multiscale finite element method for elliptic problems with oscillating coefficients. Math. Comput. **72**, 541–576 (2002) (electronic)
9. Christie, M., Blunt, M.: Tenth spe comparative solution project: a comparison of upscaling techniques. SPE Reserv. Evalu. Eng. **4**, 308–317 (2001)
10. E, W.: Homogenization of linear and nonlinear transport equations. Commun. Pure Appl. Math. **XLV**, 301–326 (1992)
11. Efendiev, Y., Ginting, V., Hou, T., Ewing, R.: Accurate multiscale finite element methods for two-phase flow simulations. J. Comput. Phys. **220**, 155–174 (2006)
12. Efendiev, Y.R., Durlofsky, L.J.: Numerical modeling of subgrid heterogeneity in two phase flow simulations. Water Resour. Res. **38**(8), 1128 (2002)
13. Efendiev, Y.R., Durlofsky, L.J., Lee, S.H.: Modeling of subgrid effects in coarse scale simulations of transport in heterogeneous porous media. Water Resour. Res. **36**, 2031–2041 (2000)
14. Efendiev, Y.R., Popov, B.: On homogenization of nonlinear hyperbolic equations. Commun. Pure Appl. Math. **4**(2), 295–309 (2005)
15. Hou, T.Y., Westhead, A., Yang, D.P.: A framework for modeling subgrid effects for two-phase flows in porous media. SIAM Multiscale Model. Simul. **5**(4), 1087–1127 (2006)
16. Hou, T.Y., Wu, X.H.: A multiscale finite element method for elliptic problems in composite materials and porous media. J. Comput. Phys. **134**, 169–189 (1997)
17. Hou, T.Y., Xin, X.: Homogenization of linear transport equations with oscillatory vector fields. SIAM J. Appl. Math. **52**, 34–45 (1992)
18. Hughes, T., Feijoo, G., Mazzei, L., Quincy, J.: The variational multiscale method—a paradigm for computational mechanics. Comput. Methods Appl. Mech. Eng. **166**, 3–24 (1998)
19. Jenny, P., Lee, S.H., Tchelepi, H.: Multi-scale finite volume method for elliptic problems in subsurface flow simulation. J. Comput. Phys. **187**, 47–67 (2003)
20. Jenny, P., Lee, S.H., Tchelepi, H.: Adaptive multi-scale finite volume method for multi-phase flow and transport in porous media. Multiscale Model. Simul. **3**, 30–64 (2005)
21. Matache, A.-M., Schwab, C.: Homogenization via *p*-FEM for problems with microstructure. In: Vichnevetsky, R., Flaherty, J.E., Hesthaven, J.S., Gottlieb, D., Turkel, E. (eds.) Proceedings of the Fourth International Conference on Spectral and High Order Methods (ICOSAHOM 1998) (Herzliya), vol. 33, pp. 43–59. Elsevier, Amsterdam (2000)
22. Sangalli, G.: Capturing small scales in elliptic problems using a residual-free bubbles finite element method. Multiscale Model. Simul. **1**, 485–503 (2003) (electronic)
23. Strinopoulos, T.: Upscaling of immiscible two-phase flows in an adaptive frame. Ph.D. thesis, California Institute of Technology, Pasadena (2005)
24. Tartar, L.: Nonlocal effects induced by homogenization. In: Culumbini, F., et al. (eds.) PDE and Calculus of Variations, pp. 925–938. Birkhfiuser, Boston (1989)
25. Wen, X., Durlofsky, L., Edwards, M.: Upscaling of channel systems in two dimensions using flow-based grids. Transp. Porous Media **51**, 343–366 (2003)
26. Westhead, A.: Upscaling two-phase flows in porous media. Ph.D. thesis, California Institute of Technology, Pasadena (2005)